Nano Research

Open Access

Research Article

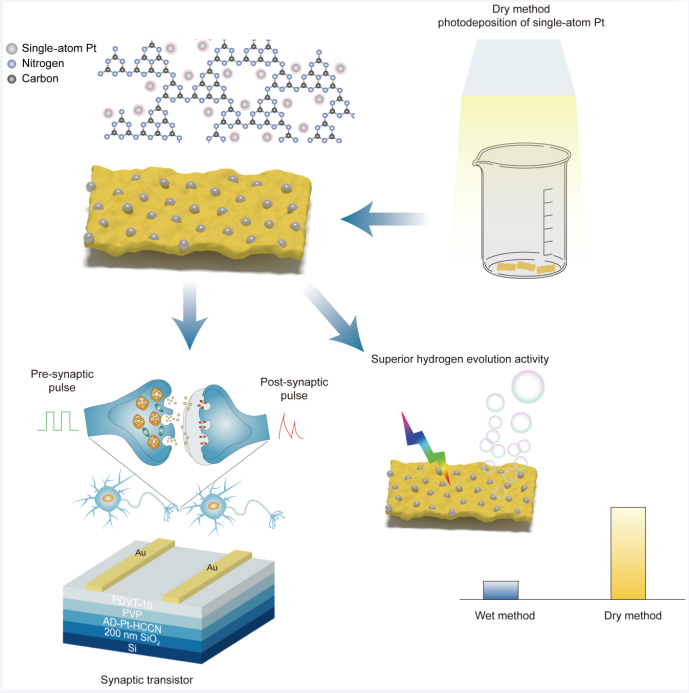
# Dry-state single-atom Pt engineering on crystalline carbon nitride for integrated hydrogen evolution and neuromorphic computing

Yongfeng Lu[1,§], Xinxin Zhuo[1,§], Wenhao Sun[1,2,§], Chuiying Yang[3], Jingwen Pan[2,4], Mikaela Görlin[2], Alexandre Holmes[5], Ergang Wang[5], Xiao Fang[1], Zihan Zhang[6], Rajeev Ahuja[6], Wei Luo[6], Huipeng Chen[3] ✉, Jiefang Zhu[2,7] ✉, and Yuanhui Zheng[1,8] ✉

[1] *College of Chemistry, Fuzhou University, Fuzhou 350116, China*
[2] *Department of Chemistry–Ångström, Ångström Laboratory, Uppsala University, SE-75121, Uppsala, Sweden*
[3] *Institute of Optoelectronic Display, National & Local United Engineering Lab of Flat Panel Display Technology, Fuzhou University, Fuzhou 350002, China*
[4] *College of School of Materials Science and Engineering, Harbin Institute of Technology, Harbin 150001, China*
[5] *Department of Chemistry and Chemical Engineering, Chalmers University of Technology, Göteborg SE-412 96, Sweden*
[6] *Materials Theory, Department of Physics and Astronomy, Uppsala University, SE-75121, Uppsala, Sweden*
[7] *The Key Laboratory for Ultrafine Materials of The Ministry of Education, East China University of Science and Technology, Shanghai 200237, China*
[8] *Fujian Provincial Key Laboratory of Advanced Inorganic Oxygenated Materials, College of Chemistry, Fuzhou University, Fuzhou 350108, China*
§ *Yongfeng Lu, Xinxin Zhuo, and Wenhao Sun contributed equally to this work.*

**Cite this article:** *Nano Research*, **2026**, *19*, 94908796. https://doi.org/10.26599/NR.2026.94908796

**ABSTRACT:** Precise construction of high-density single-atom active centers on polymeric semiconductors, together with concurrent regulation of their interfacial charge-transfer behavior, remains a central challenge for both photocatalytic energy conversion and neuromorphic electronics. Yet conventional wet photodeposition routes suffer from solvent-induced coordination distortion, defect formation, and limited metal dispersion. Here, we report a solvent-free dry-state *in situ* photoreduction strategy that anchors atomically dispersed Pt onto highly crystalline carbon nitride (AD-Pt-HCCN), achieving a Pt precursor conversion efficiency of 70.5%, which is 5.5 times higher than that of wet photodeposition. High-angle annular dark-field scanning transmission electron microscopy (HAADF-STEM), X-ray photoelectron spectroscopy (XPS), and X-ray absorption fine structure (XAFS) collectively confirm uniformly distributed Pt single atoms coordinated in a quasi-fivefold configuration within triazine-heptazine frameworks. This coordination environment suppresses the formation of a classical nanoparticle-induced Schottky-type barrier and promotes ultrafast interfacial charge extraction, as supported by femtosecond transient absorption (fs-TA), photoluminescence (PL), time-resolved PL (TRPL), and electrochemical impedance spectroscopy (EIS) analyses. As a result, a photocatalytic $H_2$ evolution rate of 5.8 mmol·g$^{-1}$·h$^{-1}$ is achieved, outperforming the counterpart prepared by conventional wet photodeposition (3.8 mmol·g$^{-1}$·h$^{-1}$), owing to the synergistic contributions of the increased Pt loading efficiency and the enhanced interfacial charge transfer




**Received:** February 9, 2026; **Revised:** April 10, 2026; **Accepted:** April 30, 2026

✉Address correspondence to Huipeng Chen, hpchen@fzu.edu.cn; Jiefang Zhu, Jiefang.Zhu@kemi.uu.se; Yuanhui Zheng, Yuanhui.Zheng@fzu.edu.cn

induced by atomically dispersed Pt sites. Remarkably, the same atomic Pt sites serve as efficient charge-modulation centers in neuromorphic transistors, enabling pronounced excitatory postsynaptic current (EPSC)/inhibitory postsynaptic current (IPSC) responses, robust long-term potentiation/depression (LTP/LTD), and linear, hardware-relevant synaptic weight updates. Integrating experimentally extracted conductance states into an artificial neural network (ANN) framework yields high recognition accuracy of 98.6%, highlighting the broad potential of AD-Pt-HCCN as a multifunctional building block for energy-intelligence convergence.

**KEYWORDS:** photocatalytic hydrogen production, highly crystalline carbon nitride, Pt, atomic dispersion, artificial synapse

## 1 Introduction

Nanoscale optoelectronic materials play essential roles in renewable energy conversion, intelligent electronics, and neuromorphic computing [1–7]. In particular, two-dimensional polymeric semiconductors, such as graphitic carbon nitride (g-$C_3N_4$) and its derivatives, owing to their tunable electronic structures, abundant surface-active sites, and excellent chemical stability, have been widely explored in photocatalytic hydrogen evolution, photodetectors, memristive devices, and artificial synapses [8–11]. Precise modulation of their structure, charge-transport pathways, and functional interfaces is critical for advancing next-generation energy conversion systems and high-efficiency computing hardware [12, 13]. However, the intrinsic localized states, interfacial defects, and sluggish carrier dynamics of polymeric semiconductors still hinder their performance in complex processes requiring efficient charge separation (e.g., photocatalytic $H_2$ evolution) or strong electric-field regulation (e.g., synaptic plasticity) [2, 8, 9, 12–14]. Consequently, introducing single-atom active centers and constructing efficient charge trapping/release architectures have emerged as promising strategies to overcome these limitations.

Recent advances in photodeposition and reduction-based single-atom deposition methods have attempted to anchor noble metal atoms on g-$C_3N_4$, yet wet routes inevitably introduce solvent molecules, reductants, and adsorbed ions [15–19]. These undesired species alter local coordination, create defect states, and obstruct charge-transfer pathways. More critically, the maximum metal dispersion achievable by solution-based methods remains fundamentally constrained by nucleation-growth kinetics, making it challenging to obtain high-density single atoms but forming clusters or nanoparticles (NPs) [17]. Such limitations not only reduce the attainable loading efficiency of catalytically active Pt species but also weaken the interfacial charge-transfer enhancement that atomically dispersed metal sites are expected to provide. As a result, the catalytic $H_2$ evolution activity of g-$C_3N_4$ and its emerging application as an artificial synaptic material both remain far below their theoretical limits. Achieving a scalable, solvent-free, high-precision approach to deposit metal single atoms on g-$C_3N_4$ thus represents a critical yet unmet challenge.

Beyond its well-established role in photocatalytic water splitting, g-$C_3N_4$ has recently gained momentum as an active layer for neuromorphic transistors owing to its intrinsic ionic gating capability, defect-mediated charge trapping, and optoelectronic plasticity [8, 9]. In neuromorphic systems, modulating charge transport and interfacial polarization under low operating voltages is essential for achieving brain-inspired behaviors, such as excitatory postsynaptic current (EPSC)/inhibitory postsynaptic current (IPSC) modulation, short-term plasticity (STP), long-term potentiation/depression (LTP/LTD), and learning–forgetting–relearning cycles [20–27]. However, pristine g-$C_3N_4$ suffers from sluggish carrier mobility, limited exciton dissociation, and suboptimal interfacial energetics, thereby restricting its synaptic response amplitude and long-term stability. A material platform capable of concurrently enhancing photoexcitation dynamics, boosting charge transfer, and stabilizing defect states would therefore be highly desirable for next-generation neuromorphic computing.

Precise engineering of metal–nitrogen coordination environments in g-$C_3N_4$ can simultaneously modulate its surface catalytic sites and electronic band structure, offering a universal route to enhance both photocatalytic and neuromorphic functionalities. Single Pt atoms, in particular, are known to create localized dipoles, lower the work function, and accelerate charge extraction—effects that are beneficial not only for hydrogen evolution but also for controlling synaptic weight changes in memristive or transistor-type synapses. Yet, achieving uniform, scalable, and ligand-free deposition of Pt single atoms onto g-$C_3N_4$ remains technically challenging with conventional wet routes. Therefore, the key scientific problem addressed here is whether a solvent-free single-atom engineering strategy can simultaneously maximize Pt atomic utilization and tailor interfacial charge-transfer pathways in carbon nitride, thereby supporting both catalytic and neuromorphic functionalities.

Herein, we present a solvent-free dry atomization strategy to anchor atomically dispersed Pt onto highly crystalline carbon nitride (AD-Pt-HCCN). This ligand-free route eliminates solvent interference and boosts Pt loading efficiency by 5.5-fold over wet photodeposition, yielding uniformly dispersed single-atom sites with high structural fidelity. By constructing a well-defined Pt–$N_x$ coordination environment that lowers the local work function and optimizes band-edge alignment, the dry method enables g-CN to function as a unified platform for both catalytic and neuromorphic processes that rely on efficient charge generation, extraction, and interfacial regulation. Accordingly, the hydrogen evolution reaction (HER) enhancement in AD-Pt-HCCN should be understood as arising from both the increased population of accessible Pt active centers and the improved interfacial charge-transfer kinetics induced by their atomic dispersion. Consequently, AD-Pt-HCCN delivers substantially enhanced hydrogen evolution activity and markedly amplified synaptic behaviors, including larger EPSC/IPSC responses and robust LTP/LTD under repeated pulses. Benefiting from the synergistic photo-electrical modulation, our neuromorphic synaptic device exhibits tunable recognition performance and achieves an accuracy of 98.6% under optimized illumination. This work demonstrates a scalable, dry-processed single-atom material that enables both efficient photocatalytic hydrogen evolution and high-performance neuromorphic computing, highlighting the potential of single-atom catalysts (SACs) as multifunctional building blocks for next-generation artificial intelligence (AI)–energy-integrated technologies.

## 2 Experimental

### 2.1 Materials

All chemicals were obtained and used as received without additional purification. Ultrapure water was prepared using a lab-grade water purification system (Arium Mini, Sartorius). Lithium chloride (LiCl, Anhydrous, analytical reagent (AR) grade) and dicyandiamide ($C_2H_4N_4$, 99%) were purchased from Shanghai Aladdin Bio-Chem Technology Co., Ltd. Additionally, sodium chloride (NaCl, AR grade), potassium chloride (KCl, AR grade), ethanol (AR grade), triethanolamine (TEOA, AR grade), and chloroplatinic acid hexahydrate ($H_2PtCl_6{\cdot}6H_2O$, AR grade) were purchased from Sinopharm Chemical Reagent Co., Ltd. (Shanghai).

### 2.2 Catalysts preparation

#### *2.2.1 Synthesis of g-$CN_x$ photocatalysts*

The light-yellow bulk g-$CN_x$ was synthesized via thermal polymerization of dicyandiamide [1, 28, 29]. Typically, 3 g of dicyandiamide, serving as a precursor, was placed in a 15 mL alumina crucible with a lid. The alumina crucible was then transferred to a tube furnace, where the dicyandiamide was calcined at 550 °C for 4 h under a $N_2$ atmosphere, with a heating ramp of 5 °C·$min^{-1}$. The resulting product was a light-yellow solid, identified as bulk g-$CN_x$.

#### *2.2.2 Synthesis of HCCN photocatalysts*

Subsequently, the yellow bulk g-$CN_x$ (0.8 g) was ground with 0.55 g of KCl and 0.45 g of LiCl into a fine powder. The mixture was heated at 100 °C for 30 min to eliminate absorbed water. Then, the temperature was raised to 550 °C with a ramp of 5 °C·$min^{-1}$ and maintained for 4 h in a $N_2$ atmosphere for further polymerization. After cooling to room temperature, the product was rinsed with water to remove lithium and potassium ions. After vacuum filtration and drying at 60 °C, the HCCN was obtained.

#### *2.2.3 Preparation of HCCN photocatalyst with atomically dispersed Pt*

HCCN (30 mg) was dispersed in ultrapure water (15 mL) via 3 min sonication, followed by 5 min magnetic stirring to form a homogeneous colloidal solution. Subsequently, 1 mL of chloroplatinic acid solution ($H_2PtCl_6{\cdot}6H_2O$) with a concentration of 0.6 mg·$mL^{-1}$ was dropwise added to the dispersion. After stirring for 5 min, the mixture was dried on a heating plate at 60 °C, yielding a uniformly distributed thin layer of powder at the bottom of the beaker. To reduce the $PtCl_4^{2-}$ ions to AD-Pt co-catalyst on the HCCN, the thin layer of HCCN powder was subjected to an *in situ* photoreduction without any further processing. The photoreduction was carried out by illuminating the thin layer of HCCN powder with a solar simulator for 1 h. The resultant powder was denoted as AD-Pt-HCCN.

#### *2.2.4 Preparation of Pt nanoparticles dispersed HCCN (NP-Pt-HCCN)*

For comparison, a traditional *in situ* photoreduction method was employed to prepare Pt nanoparticles dispersed HCCN (NP-Pt-HCCN). Typically, 30 mg of HCCN was added to a 100 mL aqueous solution containing 10 vol.% TEOA. 1 mL of $H_2PtCl_6{\cdot}6H_2O$ solution with a concentration of 0.6 mg·$mL^{-1}$ (the same amount as used for AD-Pt-HCCN) was added to the solution as the Pt precursor. The resulting mixture was purged with Ar for 30 min to remove dissolved oxygen, followed by repeated vacuum cycles within the photocatalytic system. The suspension was illuminated for 1 h. Upon completion of the reaction, the NP-Pt-HCCN was obtained.

### 2.3 Characterization

The X-ray diffraction (XRD) patterns of the HCCN, AD-Pt-HCCN, and NP-Pt-HCCN were recorded on an X-ray diffractometer (Rigaku Ultima IV 285) using Cu K$\alpha$ ($\lambda$ = 0.154 nm) as the radiation source. Microstructures and elemental mapping of AD-Pt-HCCN and NP-Pt-HCCN were characterized via a high-resolution field emission scanning electron microscope (FE-SEM, Zeiss LEO 1550) equipped with an energy-dispersive X-ray spectroscopy (Oxford AZtec EDS). Transmission electron microscopy (TEM), selected area electron diffraction (SAED), high-angle annular dark-field (HAADF) imaging in scanning TEM (STEM) mode, and EDS were performed on an FEI Titan Themis 200 microscope, equipped with a spherical aberration-corrected probe and a SuperX X-ray detector. For sample preparation, the powders were dispersed in ethanol and sonicated for 1 min. Subsequently, a small drop of the resulting solution was dropped onto a copper grid covered with a lacey carbon film. The grid was then positioned in a desiccator to allow the water to evaporate completely. The accurate content of Pt in AD-Pt-HCCN and NP-Pt-HCCN was determined by inductively coupled plasma atomic emission spectrometry (ICP-AES, LEEMAN-20165303, USA). The ultraviolet–visible (UV–Vis) absorption spectra of the samples were recorded using an ultraviolet–visible–near-infrared diffuse reflectance spectrophotometer (DRS, Varian Co. Cary-500).

Steady-state fluorescence spectra were acquired using a SPEX Fluorolog fluorimeter with an excitation wavelength of 380 nm. Emission spectra were collected with an integration time of 0.5 s and a monochromator slit width of 8 nm. Time-resolved fluorescence decays were measured with a time-correlated single photon counting (TCSPC) on a lifetime spectrofluorometer (LifeSpec II, Edinburgh Analytical Instruments). The excitation wavelength was set at 377 nm, and the emission wavelength was 464 nm. Fittings of emission decays were performed using the software (F900 from Edinburgh Instruments). X-ray photoelectron spectroscopy (XPS) and valence band XPS analysis were performed on an X-ray photoelectron spectrometer (Kratos AXIS Supra+) equipped with a monochromatized Al K$\alpha$ X-ray source (1486.6 eV). Binding energies were calibrated according to the C 1s peak at 284.8 eV. The work function of the instrument was 4.5 eV.

X-ray absorption spectroscopy (XAS) was conducted at the Pt $L_3$-edge under ambient conditions at the KMC-3 beamline of BESSY II, Helmholtz Zentrum Berlin (HZB). Spectra were collected in fluorescence mode using a 13-element Si-drift detector (RaySpec) over an energy range of 0–560 eV (equivalent to a photoelectron wave vector ($k$)-range of 0–12 $Å^{-1}$). A metallic Pt foil was used for energy calibration. Local atomic parameters, including coordination distance ($R$), coordination number (CN), and Debye–Waller factor ($\sigma^2$), were extracted via FEFF simulations and the SimXLite software developed by Holger Dau and Petko Chernev at Free University of Berlin [30]. Further details are provided in the Electronic Supplementary Material (ESM). The extended X-ray absorption fine structure (EXAFS) spectra were fitted in the $k$-space by the SimXLite software [30].

Fourier transform infrared (FTIR) measurements were carried out using a Nicolet-iS50 FTIR spectrometer from Thermo Scientific Co., equipped with an attenuated total reflectance (ATR) accessory at room temperature. FTIR spectra were recorded from 4000 to 650 $cm^{-1}$ with a resolution of 4 $cm^{-1}$, using 64 scans for each spectrum.

Electrochemical analysis was carried out in a three-electrode system, with a Pt plate as the counter electrode and an Ag/AgCl electrode as the reference electrode. The working electrode was prepared on a fluorine-doped tin oxide (FTO) glass that had been cleaned through sonication in ethanol for 3 min, and dried at 60 °C. The boundary of the FTO glass was protected using Scotch tape. The exposed area of the working electrode was 0.25 $cm^2$. A 10 mg sample was dispersed in 1 mL of ultrapure water by sonication to obtain a slurry. The sample slurries were dripped onto the pre-treated FTO glass. After the working electrode was dried in air. The Scotch tape was removed. Electrochemical impedance spectroscopy (EIS) was conducted using an electrochemical workstation (PARSTAT 3000A-DX Bipotentiostat from Princeton Applied Research, USA) in a 0.01 M $K_3[Fe(CN)_6]/K_4[Fe(CN)_6]$ (1:1) solution.

Transient absorption (TA) measurement. TA measurements were conducted using a Yb:KGW amplifier (Pharos, Light Conversion) combined with a pump-probe system (Harpia, Light Conversion). The fundamental laser (1030 nm, ~ 190 fs, 89 kHz) from the amplifier was split into two beams. One beam was used to pump an optical parametric amplifier (Orpheus, Light Conversion) and a second harmonic generator (Lyra, Light Conversion) to generate tunable pump pulse. The other 1030 nm beam was focused into a sapphire crystal to produce white light continuum as probe pulse. The pump and probe pulses were focused and overlapped onto the sample. The transmitted probe pulse was dispersed by a monochromator (Andor Kymera 193i) and detected by a silicon-based array detector. The pump-probe delay can be up to ~ 8 ns, controlled by a delay line.

### 2.4 Theoretical calculation method

First-principles calculations of structure optimizations and electron density were carried out based on density functional theory (DFT) using the Vienna *ab initio* simulation package (VASP 6). The generalized gradient approximation (GGA) was chosen as exchange-correlation functional by Perdew–Burke–Ernzerhof (PBE). The projector augmented plane wave approximation was used as pseudopotential to describe electron–ion interactions, where valence electrons $5d^9 6s^1$, $2s^2 2p^3$, $2s^2 2p^2$, and $1s^1$ were considered for elements Pt, N, C, and H, respectively. The plane wave cut-off energy and the Monkhorst–Pack *k*-spacing value were set to 400 eV and 0.03 × 2π $Å^{-1}$, respectively. The van der Waals effects were considered by the DFT-D3 method. The electronic density of states (DOS) of Pt-doped triazine-heptazine HCCN was calculated using the Heyd–Scuseria–Ernzerhof screened hybrid functional (HSE06), which accounts for nonlocal exchange effects.

### 2.5 Photocatalytic $H_2$ production

Photocatalytic $H_2$ production by AD-Pt-HCCN and NP-Pt-HCCN was performed under top illumination in a quartz reaction vessel connected to a closed gas circulation system. A 300 W Xe arc lamp (PLS-SEX300D, Beijing Perfect Light Co., Ltd.) equipped with a UV cut-off filter ($\lambda$ > 420 nm) was used as the illumination source. The temperature of the photocatalytic reaction was controlled at 5 °C via recirculating water from a low-temperature bath (DC-1006A, Shanghai Hengping Co., Ltd.). The evolved gas was analyzed using an online gas chromatograph (Shimadzu GC-2014C+AT 230C) equipped with a thermal conductivity detector (TCD) and Ar as the carrier gas. The prepared photocatalysts (30 mg) were dispersed in 100 mL an aqueous solution containing 50 mg NaCl and 10 mL TEOA as the hole-scavenging agent. The mixture was then sealed and evacuated for 30 min. Subsequently, the mixture was illuminated while being stirred. Both AD-Pt-HCCN and NP-Pt-HCCN underwent continuous photocatalytic $H_2$ evolution tests for 20 h, with each sample tested three times. The average activity, along with the standard deviation, was used to present the results. The reaction system was evacuated for 30 min after each 5 h interval before proceeding to the next photocatalytic cycle, until a total reaction time of 20 h was achieved. Following the 20 h test, the reaction vessel was vented to expose the solution to air for 30 min, evacuated again for 30 min, and subjected to an additional 5 h photocatalytic test to evaluate the reactivation of $H_2$ evolution performance [31]. For AD-Pt-HCCN, after the 25 h photocatalytic test, an additional 10 mL of TEOA was added to the solution. Subsequently, a 5 h photocatalytic $H_2$ evolution test was carried out to assess the photocatalytic stability of AD-Pt-HCCN. The procedure is shown in Fig. S17 in the ESM.

### 2.6 Device fabrication

A 1.4 cm × 1.4 cm Si wafer with a thermally grown 200 nm $SiO_2$ layer was sequentially cleaned with acetone, isopropanol, and deionized water. Dispersions of HCCN and AD-Pt-HCCN (2 mg·$mL^{-1}$ in N,N-dimethylformamide (DMF)) were ultrasonically exfoliated and filtered through a 0.22 μm needle filter. Subsequently, 200 μL of each colloidal dispersion was drop-cast onto the wafer and spin-coated at 2000 rpm for 60 s, followed by annealing at 80 °C for 20 min. A polyvinyl pyrrolidone (PVP) layer (15 mg·$mL^{-1}$ in DMF) was then deposited in a nitrogen-filled glove box by spin-coating 200 μL of solution at 2000 rpm for 30 s and annealed at 120 °C for 2 h. Next, 200 μL of a fully dissolved PDVT-10 (the structure shown in Fig. S18 in the ESM) solution was spin-coated at 1000 rpm for 30 s and thermally annealed at 150 °C for 10 min. Finally, high-purity Au was thermally evaporated under high vacuum to form 50 nm-thick top electrodes.

### 2.7 Artificial neural network (ANN) training procedure

During training, pixel-level intensities from the preprocessed images were first vectorized to generate the input vector ($X_m$). This vector was sequentially propagated through a multi-layer perceptron architecture comprising progressively compressed hidden layers. The synaptic coefficients in each layer were mapped from the normalized multilevel conductance states obtained from the LTP/LTD characteristics of the fabricated neuromorphic transistor, thereby ensuring that the network operated under hardware-relevant weight constraints.

Within this architecture, each hidden layer performed nonlinear feature extraction, while intermediate activation functions enabled hierarchical refinement of representations. The deeper multi-layer topology demonstrated superior classification accuracy compared with the shallow configuration. This enhancement arises from two synergistic mechanisms: (i) Progressive dimensionality reduction mitigates the information loss that typically accompanies single-step compression, allowing the network to extract increasingly discriminative subspaces; and (ii) in quantized hardware-aware

networks, the discrete synaptic weights introduce perturbations that shallow architectures cannot effectively compensate. In contrast, the deeper structure, supported by successive nonlinear transformations, efficiently absorbs and recalibrates these quantization-induced distortions, yielding more stable feature embeddings and better-defined decision boundaries.

During optimization, the network parameters were iteratively updated by minimizing the error between predicted outputs and ground-truth labels. The final output vector ($Y_m$) corresponding to digits "0"–"9" was generated after the activation function in the output layer. To ensure a rigorous evaluation of model generalization, all test images were strictly excluded from the training phase and were used solely for final benchmarking. The recognition accuracy was quantified by directly comparing the predicted classes with the labels of the evaluation dataset.

## 3 Results and discussion

### 3.1 Dry-deposited single-atom Pt-HCCN enabling dual-functional photocatalysis and neuromorphic electronics

In the conventional wet photoreduction process (Fig. S1(a) in the ESM), $PtCl_6^{2-}$ species are dissolved in the reaction solution and can migrate freely to the photocatalyst surface. Upon illumination, the initially reduced Pt species tend to form metallic nuclei, which then serve as electron-enriched growth centers for further Pt deposition. This solution-phase nucleation-and-growth pathway therefore favors the formation of Pt nanoparticles. In contrast, in the dry photodeposition strategy presented in this work, $H_2PtCl_6$ is first introduced into the HCCN suspension and, after solvent evaporation, $PtCl_6^{2-}$ species remain anchored on the HCCN surface. The detailed synthesis procedure of AD-Pt-HCCN is illustrated in Fig. 1(a) and Fig. S1(b) in the ESM. As a result, the Pt precursor is spatially confined at surface active sites before photoreduction. Under subsequent light irradiation, the reduction of these immobilized Pt species is more likely to occur locally at the anchoring sites, while the absence of liquid-phase diffusion significantly suppresses Pt–Pt migration, encounter, and coalescence. Therefore, compared with wet photodeposition, the dry process is more favorable for generating highly dispersed, atomically distributed Pt species rather than metallic Pt nanoparticles. In addition, the protons from the $H_2PtCl_6{\cdot}6H_2O$ could insert into the graphite-like interlayers of HCCN, which facilitated the exfoliation of bulk HCCN into thin layers, thereby further increasing the adsorption area for Pt atoms [28]. These combined effects explain the distinct Pt states obtained from the two photodeposition routes.

Benefiting from this engineered atomic interface, the AD-Pt-HCCN catalyst exhibits markedly improved hydrogen evolution

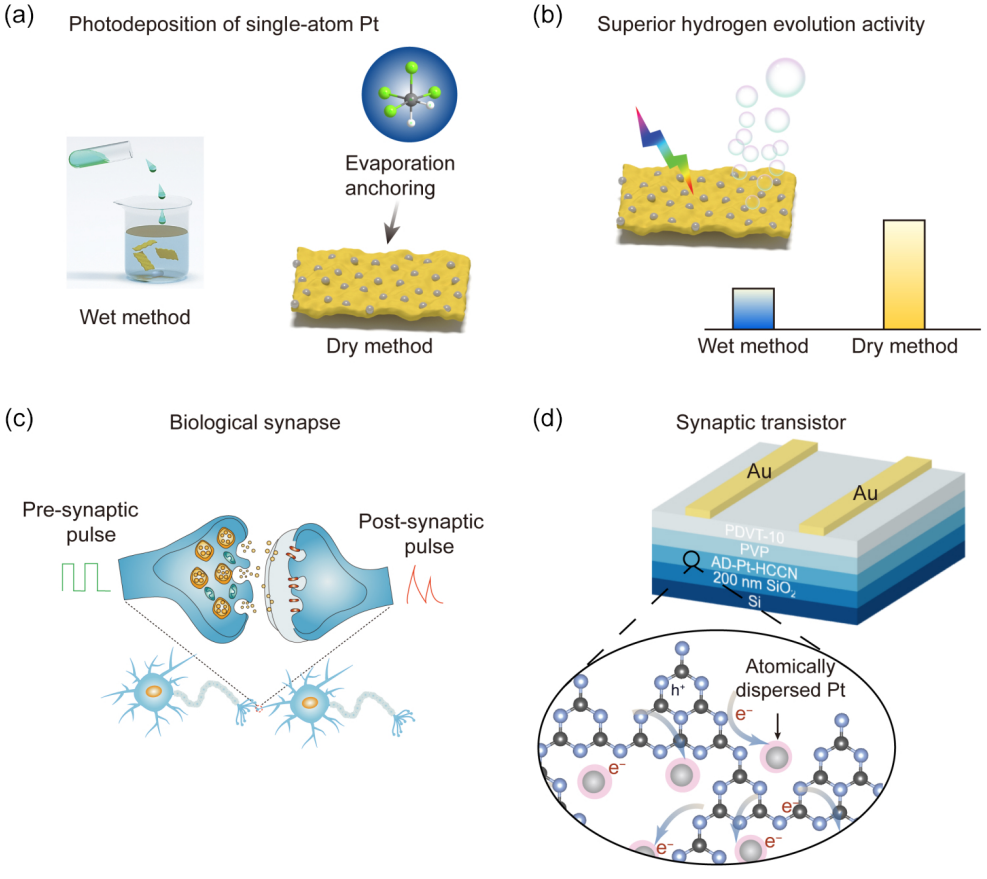



**Figure 1** Dry-deposited single-atom Pt on crystalline carbon nitride for enhanced photocatalysis and neuromorphic applications. (a) Comparison between the traditional wet photodeposition and the dry evaporation-anchoring strategy developed in this work. The dry method enables solvent-free anchoring of atomically dispersed Pt onto HCCN, effectively minimizing Pt aggregation. (b) Illustration of the superior hydrogen evolution performance of dry-deposited Pt-HCCN compared with wet-prepared samples, originating from improved charge extraction efficiency and maximized atomic utilization of Pt. (c) Schematic of the biological synapse. (d) Schematic of the synaptic transistor based on AD-Pt-HCCN. Atomically dispersed Pt sites modulate charge trapping/detrapping processes, enabling key synaptic functions, such as EPSC modulation and long-term plasticity.

activity compared with its wet-deposited counterpart (Fig. 1(b)). The enhanced performance originates from maximized Pt atomic utilization, reduced charge recombination, and reinforced surface reaction kinetics. Beyond catalysis, the unique charge modulation capability of atomically dispersed Pt was applied in neuromorphic electronics (Figs. 1(c) and 1(d)). A synaptic transistor incorporating AD-Pt-HCCN as the functional layer demonstrates efficient charge trapping/detrapping dynamics, enabling biologically relevant synaptic behaviors. The device exhibits clear EPSC/IPSC modulation and synaptic plasticity, highlighting the potential of dry-deposited single-atom Pt systems in multifunctional optoelectronic and neuromorphic applications.

### 3.2 Morphology and crystallography

AD-Pt-HCCN and NP-Pt-HCCN were synthesized using the same amount of Pt precursor. ICP-AES analysis shows that the Pt loading contents of AD-Pt-HCCN and NP-Pt-HCCN are 0.531 wt.% and 0.097 wt.%, respectively. Based on the theoretical Pt mass introduced from the $H_2PtCl_6{\cdot}6H_2O$ precursor (0.226 mg), the corresponding Pt conversion efficiencies were calculated to be 70.5% for AD-Pt-HCCN and 12.6% for NP-Pt-HCCN (Table S1 in the ESM). These results indicate that the dry-state photoreduction strategy improves Pt precursor conversion efficiency by approximately 5.5 times relative to conventional wet photodeposition. Such a highly dispersed single-atom configuration is advantageous for interfacial charge-transfer regulation, as it maximizes the Pt-HCCN interfacial contact and promotes efficient carrier extraction, which is beneficial not only for photocatalytic $H_2$ evolution but also for synaptic signal modulation in neuromorphic devices.

The morphology of the AD-Pt-HCCN photocatalyst was examined via high-resolution TEM (HR-TEM). Figure 2(a) presents HR-TEM images featuring irregular nanosheets with lateral dimensions of tens of nanometers. A closer look at a magnified image of an individual particle (as shown in the inset) reveals a lattice fringe spacing of 0.94 nm, corresponding to the (100) lattice plane of HCCN [1]. Notably, no discernible Pt species are visible, suggesting that the Pt species are extremely small. To further investigate the distribution and configuration of Pt on AD-Pt-HCCN, HAADF-STEM was employed, taking advantage of its ability to detect individual heavy atoms. Figure 2(b) demonstrates that Pt atoms, appearing as bright spots, are uniformly dispersed on the AD-Pt-HCCN surface. The size distribution reveals that 98.99% of the Pt species are smaller than 0.2 nm (Fig. S2 in the ESM), indicating that Pt is predominantly present as atomically dispersed species in AD-Pt-HCCN [29]. An enlarged HAADF-STEM image (Fig. 2(c)) shows no evidence of significant nanoparticle formation, although the presence of extremely minor near-atomic aggregates cannot be completely excluded. Additionally, Figs. 2(d)–2(g) show the EDS mapping of AD-Pt-HCCN, which further validates the presence of Pt on the HCCN with uniform distribution. The Pt single atom site density was quantified to be 2.2 $nm^{-2}$, supporting the high-density Pt dispersion enabled by the dry-state photoreduction strategy. This value compares favorably with reported Pt single atom densities on carbon nitride supports (Table S2 in the ESM) [32, 33]. These results further indicate that AD-Pt species uniformly covered the surface of HCCN and that the dry photodepostion method successfully avoided the aggregation of Pt atoms. Such a highly dispersed single-atom configuration is particularly favorable for interfacial charge-transfer enhancement, because it maximizes the metal–support interfacial contact and avoids the carrier trapping and inefficient utilization typically associated with Pt nanoparticles or aggregates. The presence of oxygen on the HCCN surface may originate from adsorbed $O_2$ or from its presence as Pt oxides.

In the case of conventional photodeposition for synthesizing NP-

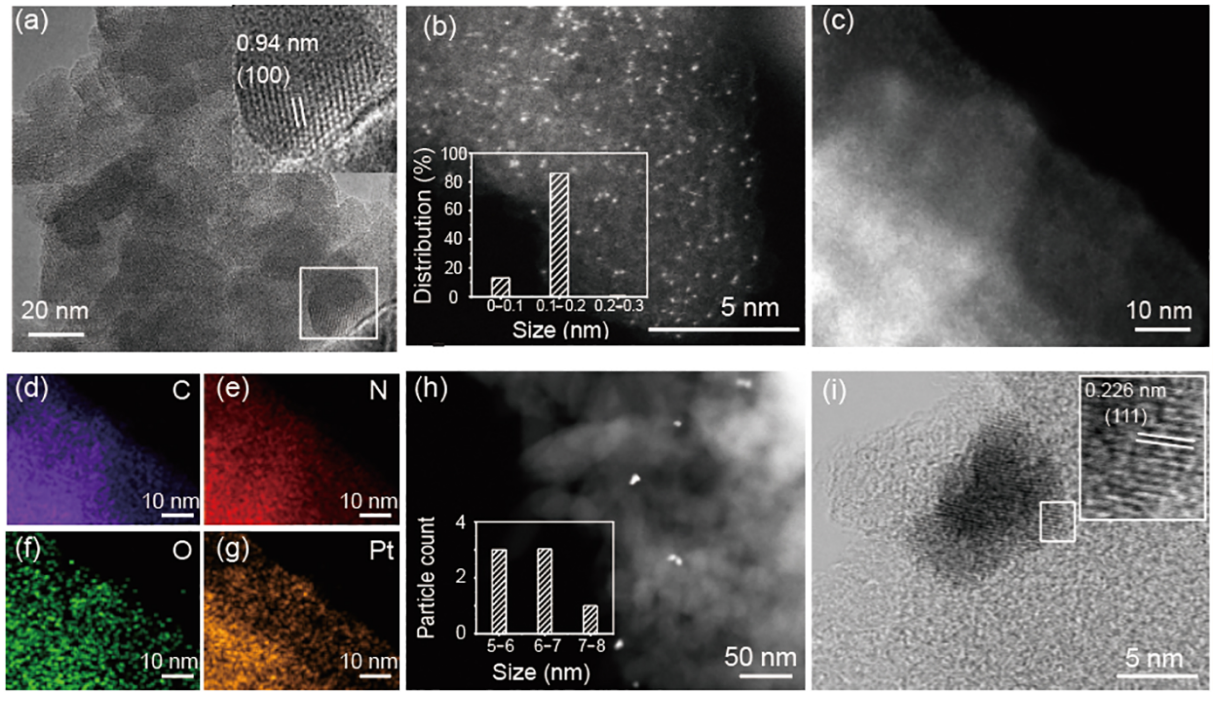



**Figure 2** Morphological comparison of AD-Pt-HCCN and NP-Pt-HCCN. (a) HR-TEM and (b) HAADF-STEM images of AD-Pt-HCCN (inset: size distribution of Pt atoms in AD-Pt-HCCN). (c) The HAADF-STEM image of AD-Pt-HCCN, and ((d)–(g)) the corresponding EDS mapping images. (h) HAADF-STEM image of NP-Pt-HCCN and the histogram of Pt NPs diameters. (i) The TEM image of NP-Pt-HCCN and corresponding lattice fringe image of a Pt nanoparticle.

Pt-HCCN, a notably distinct Pt dispersion was observed. A representative HAADF-STEM image, shown in Fig. 2(h), depicts a sparse distribution of those small, bright NPs across the host material. The enhanced brightness of these NPs compared to the HCCN matrix suggests a higher atomic number, indicating their identity as Pt NPs with diameters ranging from 5 to 7 nm. A bright-field HR-TEM image, depicted in Fig. 2(i), provides a close-up view of an individual nanoparticle on the support, displaying distinct lattice fringes with a spacing of 0.226 nm, corresponding to the (111) lattice plane of metallic Pt [34]. This confirms that the bright spots observed in the HAADF-STEM images are Pt NPs. A representative low-magnification TEM image (Fig. S3(a) in the ESM) also shows that Pt NPs, visible as black spots, are randomly and sparsely distributed on the surface of HCCN. The morphology and crystallinity of the HCCN in NP-Pt-HCCN were similar to those in AD-Pt-HCCN, with clear lattice fringes (Figs. S3(b)–S3(d) in the ESM). The diffraction rings extracted from the SAED indicated that HCCN has two interplanar distances of 0.28 and 0.94 nm, corresponding to (002) and (100) crystal planes of HCCN, respectively [35]. EDS mapping images of NP-Pt-HCCN reveal that Pt is highly localized in small clusters, whereas the elements C, N, and O are uniformly dispersed across the HCCN surface (Fig. S4 in the ESM). These results suggest that the difference in Pt species between the NP-Pt-HCCN and AD-Pt-HCCN samples originated exclusively from the photodeposition method employed. Taken together, the dry-state route not only delivers substantially higher Pt loading than the conventional wet route, but also preserves Pt in an atomically dispersed form that is more effective for interfacial charge-transfer enhancement. These two factors synergistically account for the superior overall performance of AD-Pt-HCCN, including its enhanced photocatalytic $H_2$ evolution and amplified artificial synaptic responses.

XRD patterns of pristine HCCN, AD-Pt-HCCN, and NP-Pt-HCCN show no significant shifts in peak positions (Fig. S5 in the ESM). The three samples exhibit two characteristic peaks at 8.1° and 28.2°, corresponding to the (100) in-plane repeating units of triazine-heptazine and the (002) interlayer stacking of graphitic structures, respectively [36]. Nevertheless, for AD-Pt-HCCN, the intensity of the (002) peak is noticeably reduced, indicating that the layered HCCN structure was exfoliated into thinner sheets. This was potentially facilitated by protons released from the decomposition of $H_2PtCl_6{\cdot}6H_2O$ during ultrasonication [28]. The formation of thinner HCCN nanosheets may further shorten carrier transport pathways and facilitate charge separation, which, together with the higher Pt loading efficiency and atomically dispersed Pt sites, is beneficial for interfacial photoelectronic processes involved in both photocatalysis and neuromorphic operation.

### 3.3 Chemical state analysis

To discriminate the chemical state of the Pt species in AD-Pt-HCCN and NP-Pt-HCCN, both samples were characterized using XPS. The Pt 4f spectra in Fig. 3(a) reveal distinct Pt chemical states in the two samples. NP-Pt-HCCN exhibits $Pt^0$ and Pt(II) signals, consistent with nanoparticle formation [37]. In contrast, AD-Pt-HCCN displays only Pt(II) and Pt(IV) peaks, with no detectable metallic Pt, confirming that the dry photoreduction route effectively suppresses Pt nucleation and yields oxidized, highly dispersed Pt species. The C 1s and N 1s spectra (Fig. S6 in the ESM) of AD-Pt-HCCN remain nearly identical to pristine HCCN, indicating minimal perturbation to the host framework [38, 39]. By contrast, NP-Pt-HCCN shows a shift toward higher binding energies, suggesting electron depletion caused by metallic Pt-HCCN interfacial interactions [39–41]. O 1s spectra (Fig. S7 in the ESM) show increased intensity at 531.4 eV for AD-Pt-HCCN, consistent with the presence of Pt–O species [42].

EXAFS analysis at the Pt $L_3$-edge was conducted to further characterize the electronic structure and local coordination environment of Pt. Normalized X-ray absorption near-edge structure (XANES) spectra were used to identify the electronic states of the Pt species (Fig. 3(b)). Both the white line peak areas and threshold energies ($E_0$) were comprehensively considered to analyze the electronic state and oxidation state of Pt. The details of these parameters are listed in Table S3 in the ESM. The white line area of AD-Pt-HCCN is greater than that of NP-Pt-HCCN and Pt foil, but smaller than that of the Pt(IV) reference ($Na_2Pt(IV)(OH)_6$), indicating that Pt species in AD-Pt-HCCN possess a fewer unoccupied 5d states than Pt(IV), and exist in a mixed oxidation state of Pt(II) and Pt(IV) [43]. Additionally, the $E_0$ value of AD-Pt-HCCN is lower than that of the Pt(IV) reference but higher than that of NP-Pt-HCCN. These results further indicate that the Pt in AD-Pt-HCCN exists in both Pt(II) and Pt(IV) oxidation states, consistent with the XPS results. In contrast, NP-Pt-HCCN exhibits an $E_0$ close to Pt foil and far below Pt(IV), confirming its predominantly metallic Pt(0) nature (Table S3 in the ESM).

Quantitative EXAFS fitting (Fig. 3(c) and Fig. S8 in the ESM) reveals that AD-Pt-HCCN features a dominant first-shell at an average bond length of ~ 2.0 Å with an average CN of 6.1, consistent with Pt coordinated to light elements (O, C, or N) (Table S4 in the ESM). While these light scattering atoms possess distinct phase functions, their backscattering amplitudes are sufficiently similar that EXAFS alone cannot definitely discriminate between them [29]. Furthermore, due to the strong correlation between the $\sigma^2$ and the coordination number, the $\sigma^2$ value for the first Pt–O shell was derived from a $Na_2Pt(IV)OH_6$ reference ($\sigma^2 = 0.0035$), assuming 6 oxygen ligands. Since the absolute value of CN depends strongly on $\sigma^2$, we have additionally provided EXAFS simulations where CN was fixed to 5 to match the DFT model (Table S5 in the ESM). Notably, the absence of a second coordination shell suggests that the Pt atoms are atomically dispersed, or present as near-atomic clusters on the HCCN support. This was further supported by simulations of various $PtO_2$ cluster sizes (Fig. 3(d) and Table S6 in the ESM). It should be emphasized that EXAFS provides the average contribution of all neighboring atoms around the absorbing atom (e.g., Pt) rather than reflecting the integer coordination number of individual atoms.

Here, the fitted $R$ value reflects the average Pt-neighbor bond distance, while CN represents the average number of scattering atoms surrounding Pt. The $\sigma^2$ describes the degree of local structural disorder or bond-length fluctuation, and therefore directly affects the apparent CN obtained from fitting. The $\Delta E_0$ (where $\Delta E_0$ represents the energy-zero shift between the experimental EXAFS spectrum and the theoretical model) term accounts for the energy shift between the experimental spectrum and the theoretical model, whereas the $R$-factor reflects the goodness of fit. From this perspective, the dominant first-shell contribution at ~ 2.0 Å in AD-Pt-HCCN indicates Pt coordinated primarily by light atoms rather than Pt–Pt metallic bonding. In contrast, the multiple Pt–Pt shells observed for NP-Pt-HCCN, which closely resemble those of Pt foil, are characteristic of metallic

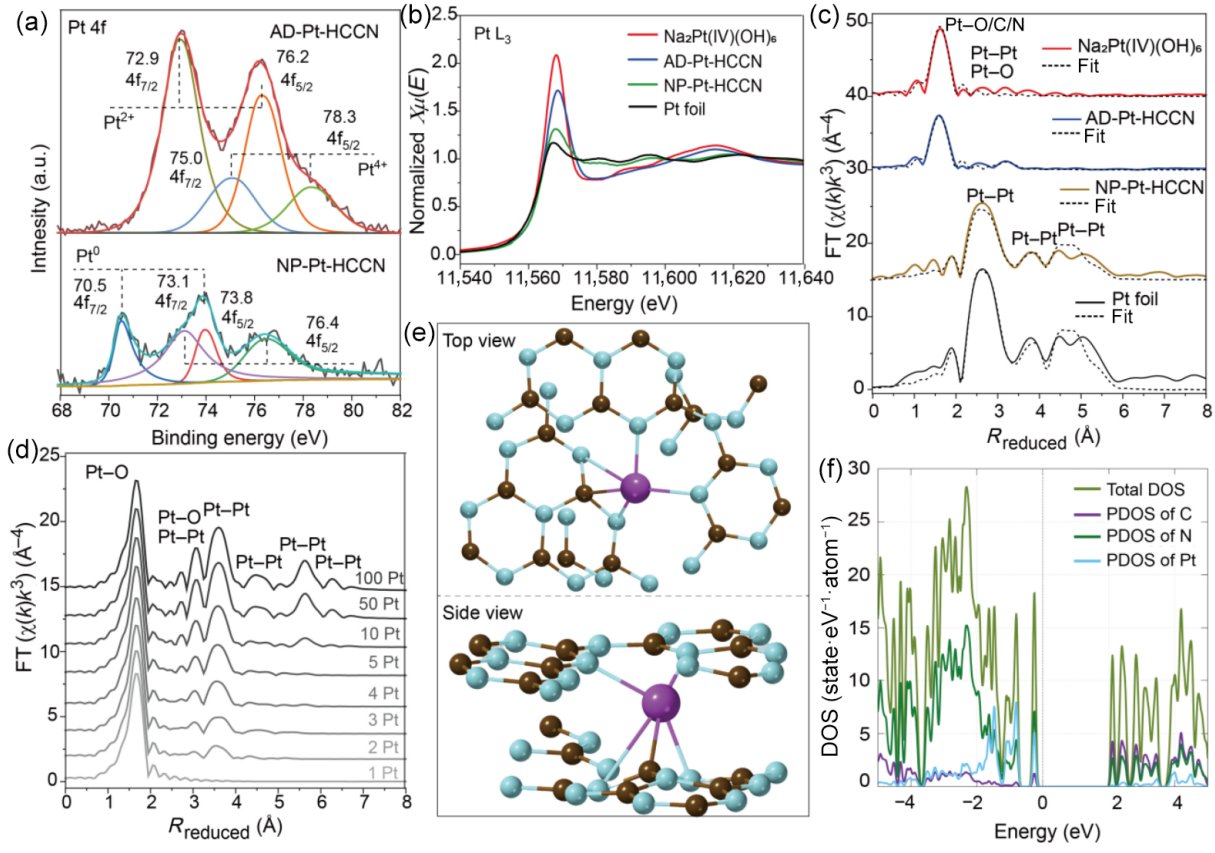



**Figure 3** XPS and synchrotron XAFS measurements. (a) XPS spectra of Pt 4f for AD-Pt-HCCN and NP-Pt-HCCN. (b) Normalized XANES spectra at the Pt $L_3$-edge for the AD-Pt-HCCN, NP-Pt-HCCN, $Na_2Pt(IV)(OH)_6$, and Pt foil. (c) FT magnitudes of Pt $L_3$-edge EXAFS spectra of AD-Pt-HCCN, NP-Pt-HCCN, $Na_2Pt(IV)(OH)_6$, and Pt foil. Black dashed lines represent the corresponding fits using FEFF simulations/modeling. (d) Simulations of various-sized Pt–O clusters shown as $k^3$-weighted FT-EXAFS in *R*-space. (e) Top and side views of the sandwich structure of AD-Pt-HCCN. Green, black, and purple spheres represent N, C, and Pt atoms. (f) Total and PDOS for the sandwich structure of AD-Pt-HCCN.

Pt nanoparticles. Therefore, the EXAFS fitting parameters in Table S4 in the ESM support the conclusion that AD-Pt-HCCN contains atomically dispersed Pt species with light-element coordination, whereas NP-Pt-HCCN contains metallic Pt nanoparticles.

Generally, due to the lone pair of electrons on the pyridine nitrogen in the triazine-heptazine ring of HCCN, the most common coordination mode for a metal element with HCCN is the bonding of the metal atom to the nitrogen atom of the triazine-heptazine ring [44, 45]. In contrast, EXAFS parameters of NP-Pt-HCCN match those of metallic Pt, validating the formation of Pt nanoparticles.

To elucidate the coordination environment and electronic structure of AD-Pt on HCCN, DFT calculations were performed to evaluate its electronic distribution, formation energy, and projected DOS (PDOS). The HCCN model consists of triazine-heptazine units linked by nitrogen (Fig. S9 in the ESM), where metal atoms preferentially anchor at edge sites. Based on these insights, a sandwich-like AD-Pt-HCCN model was constructed (Fig. 3(e)), in which a single Pt atom is simultaneously coordinated to the upper and lower triazine-heptazine layers, forming a quasi-five-coordinated configuration. Geometry optimization yielded stable Pt–N/C bonding with a formation energy of −3.94 eV (Table S7 in the ESM). The elongated $Pt–N_4$ bond (2.79 Å) suggests weaker interaction, consistent with partial charge redistribution.

Electron density analyses indicate that the valence band arises from hybridization between the quasi-five-coordinated Pt center and its neighboring atoms, while the conduction band primarily originates from the upper HCCN layer, revealing an interlayer potential gradient. The unique coordination environment endows the Pt site with catalytic electron-donating capability. The PDOS analysis (Fig. 3(f)) further shows that states near the Fermi level (0 eV) are dominated by hybridized Pt-5d and N/C-2p orbitals, with the major occupied peak below Fermi energy ($E_F$) governed by the quasi-five-coordinated Pt. The spatial confinement imposed by surrounding N and C atoms effectively "locks" the Pt center, preventing further metal attachment and thereby explaining the experimentally observed high atomic dispersion.

Importantly, this Pt-induced interfacial electronic coupling provides a unified mechanistic basis for both functionalities investigated here: It promotes directional charge transfer for photocatalytic HER, while simultaneously enabling effective charge modulation and interfacial polarization in the synaptic device.

### 3.4 Proposal of photocatalytic mechanism

During the HER tests, AD-Pt-HCCN exhibits markedly superior photocatalytic hydrogen evolution, achieving 5.8 $mmol·g^{-1}·h^{-1}$—approximately 1.5 times higher than that of NP-Pt-HCCN (3.8 $mmol·g^{-1}·h^{-1}$, Fig. S10(a) in the ESM). To place this result in context, we compared the HER performance of AD-Pt-HCCN with recently reported Pt single atom catalysts on carbon nitride supports, as summarized in Table S8 in the ESM. The HER activity of AD-Pt-HCCN is competitive among representative Pt single

atom/carbon nitride photocatalysts reported to date [46–49]. It should be noted that absolute HER rates reported in different studies are influenced by multiple experimental parameters, such as reactor configuration, catalyst dosage, light source, and sacrificial reagents; therefore, these values are not strictly directly comparable. Importantly, the superior HER activity of AD-Pt-HCCN over NP-Pt-HCCN in this work is attributed to the synergistic effects of the higher Pt loading/conversion efficiency and the enhanced interfacial charge transfer enabled by atomically dispersed Pt sites, rather than to a single factor alone. The Pt content of the recovered catalyst after long-term HER cycling was measured to be 0.635 wt.% by ICP-AES (Table S9 in the ESM). This value is slightly higher than the initial loading (0.531 wt.%) of the freshly prepared AD-Pt-HCCN, which is likely due to the further reduction and deposition of a small amount of residual Pt precursor during the prolonged photocatalytic process. Colorimetric evolution during HER further supports this: NP-Pt-HCCN remains in the blue "electron-stored" state, whereas AD-Pt-HCCN maintains the light-green "active" state, indicating more efficient consumption of photogenerated electrons (Fig. S10(b) in the ESM) [19, 31, 50, 51]. Combined with the substantially higher Pt utilization achieved by the dry-state route, these observations indicate that AD-Pt-HCCN simultaneously provides a higher density of accessible Pt active centers and more efficient electron extraction pathways during photocatalysis.

Optical analyses confirm that the performance enhancement does not arise from bandgap modulation, as HCCN maintains a bandgap of 2.7 eV (Fig. 4(a) and Fig. S11 in the ESM). In addition, FTIR spectrum (Fig. S12 in the ESM) shows the characteristic cyano absorption of ionothermally synthesized HCCN, reaffirming the integrity of the underlying carbon nitride framework [52]. The slight absorption blue shift upon Pt incorporation (Fig. S13 in the ESM) is negligible compared to the dramatic differences in charge-transfer behavior. These results further suggest that the superior HER activity of AD-Pt-HCCN is dominated by differences in Pt utilization and interfacial charge-transfer kinetics, rather than by changes in the intrinsic band structure of HCCN. Steady-state photoluminescence (PL) spectra (Fig. 4(b)) reveal substantially quenched emission for AD-Pt-HCCN, indicating efficient carrier extraction by Pt single atoms. Time-resolved PL (TRPL) measurements (Fig. 4(c)) further show significantly extended carrier lifetimes (32.3 ns for AD-Pt-HCCN vs. 19.1 ns for NP-Pt-HCCN and 1.4 ns for pristine HCCN), consistent with suppressed recombination and enhanced electron migration. To directly probe the photoinduced charge-carrier dynamics, femtosecond TA (fs-TA) spectroscopy was further performed on HCCN, NP-Pt-HCCN, and AD-Pt-HCCN (Fig. S14 in the ESM). The transient contour plots and selected delay-time spectra reveal different carrier-relaxation behaviors among the three samples. Kinetic fitting gives $\tau_1$ = 11.87 ps, $\tau_2$ = 115.2 ps, $\tau_3$ = 4883 ps (where $\tau_2$ and $\tau_3$ represent the intermediate and slow decay time constants, respectively), and $\tau_{avg}$ = 1670 ps for HCCN; $\tau_1$ = 6.732 ps, $\tau_2$ = 168.8 ps, $\tau_3$ = 9689 ps, and $\tau_{avg}$ = 3288 ps for NP-Pt-HCCN; and $\tau_1$ = 4.235 ps, $\tau_2$ = 291.1 ps, $\tau_3$ = 12,736 ps, and $\tau_{avg}$ = 4344 ps for AD-Pt-HCCN. Compared with HCCN and NP-Pt-HCCN, AD-Pt-HCCN exhibits the shortest ultrafast decay component ($\tau_1$) and the longest average lifetime ($\tau_{avg}$). The shortened ultrafast component is consistent with faster early-time electron extraction by atomically dispersed Pt sites, while the prolonged slower decay components are consistent with longer-lived charge-separated states and suppressed charge recombination [53, 54]. Electrochemical impedance spectroscopy (Fig. 4(d)) also demonstrates the smallest charge-transfer resistance for AD-Pt-HCCN, highlighting the superior conductivity pathways enabled by atomically dispersed Pt.

Mechanistically, NP-Pt-HCCN forms a classical Mott–Schottky barrier because metallic Pt nanoparticles possess a higher work

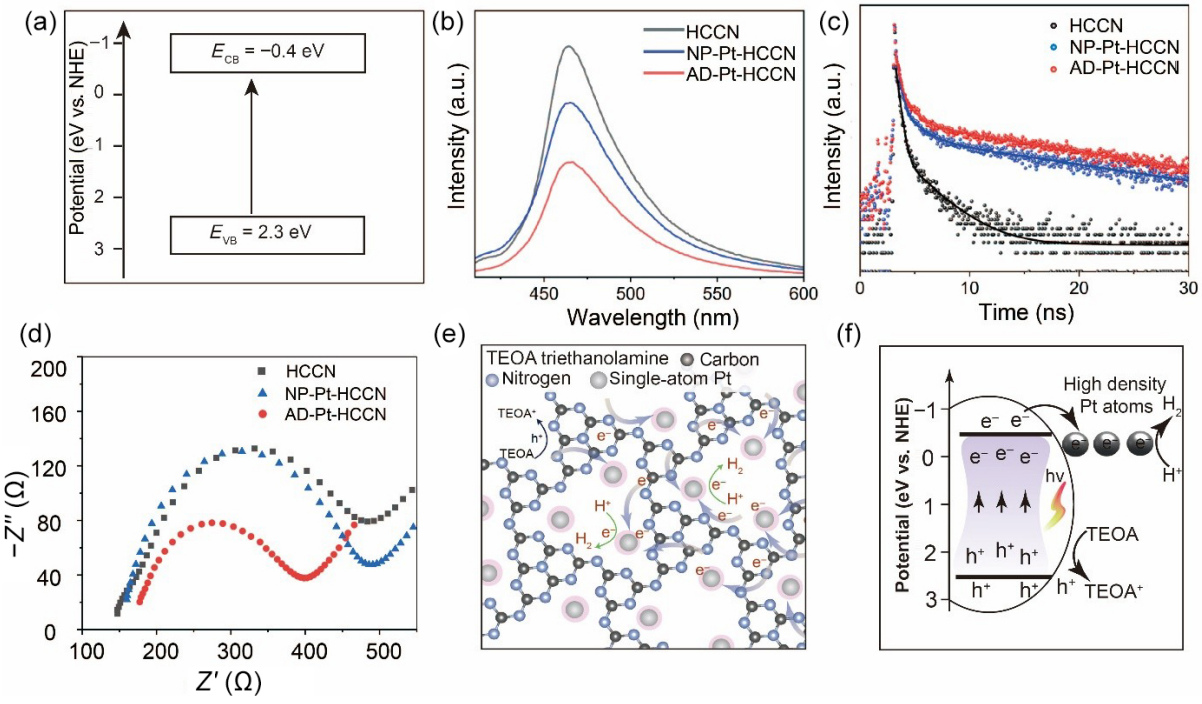



**Figure 4** Charge-transfer enhancement and HER mechanism enabled by AD-Pt-HCCN. (a) Schematic illustration of the band structure of HCCN. (b) Steady-state PL spectra and (c) TRPL spectra of HCCN, AD-Pt-HCCN, and NP-Pt-HCCN. (d) Electrochemical impedance spectra of HCCN, NP-Pt-HCCN, and AD-Pt-HCCN. (e) Atomic-scale visualization of dense electron migration pathways enabled by single-atom Pt-anchored HCCN. (f) The photocatalytic HER mechanism of AD-Pt-HCCN.

function than HCCN (Fig. S15 in the ESM) [15, 31, 55–59]. This upward band bending hinders electron flow from HCCN to Pt, consistent with the positive binding-energy shifts observed in XPS. In contrast, AD-Pt-HCCN contains isolated Pt atoms lacking a continuous metallic band structure. Strong Pt–N/C coordination disrupts the metallic density of states, generating positively polarized Pt centers without a defined metallic Fermi level. As a result, no classical Schottky barrier forms, and electrons can be extracted directly by electrophilic Pt sites. DFT calculations and EXAFS spectra collectively reveal a quasi-fivefold Pt coordination within triazine-heptazine units (Figs. 3(e) and 3(f)). This dual-layer anchoring reinforces the intrinsic polarization of HCCN and enables highly localized electron-transfer channels, forming dense "electron highways" at the interface (Fig. 4(e)). This site-selective transfer minimizes recombination and accelerates directional electron flow toward Pt, thereby boosting HER efficiency. As summarized in Fig. 4(f), atomic Pt sites catalyze proton reduction to $H_2$ while holes migrate to TEOA, and the partially oxidized Pt species may also suppress the reverse HER reaction, further enhancing activity [42, 60]. Therefore, the superior HER performance of AD-Pt-HCCN can be attributed to a dual advantage: The dry-state strategy markedly improves Pt loading efficiency, increasing the density of catalytically accessible Pt sites, while the atomically dispersed Pt–N/C coordination environment enhances interfacial charge extraction and directional electron transfer. The synergy between these two effects ultimately accounts for the markedly higher HER activity of AD-Pt-HCCN relative to NP-Pt-HCCN.

### 3.5 Application of AD-Pt-HCCN in artificial synaptic devices

These atomic-level electronic advantages are not exclusive to photocatalysis. Because synaptic computation relies on interfacial charge trapping, detrapping, and transport dynamics, the same Pt-engineered environment is expected to dramatically enhance neuromorphic behaviors. The atomically dispersed Pt sites in AD-Pt-HCCN—previously shown to accelerate charge separation and suppress Schottky barriers in photocatalysis—also play a decisive role in modulating neuromorphic behavior. Compared with pristine HCCN, the AD-Pt-HCCN synaptic transistor exhibits a substantially enlarged hysteresis window, higher channel current, and stronger gate-field sensitivity under dark and light (Fig. 5(a) and Fig. S16(a) in the ESM). These enhancements arise from Pt–$N_x$-induced regulation of localized electronic states and strengthened interfacial polarization within the AD-Pt-HCCN/PVP/PDVT-10 heterostructure. To evaluate device reproducibility, the double-sweep transfer curves of seven different devices were characterized. As shown in Fig. S16(b) in the ESM, all devices exhibit an on/off ratio of $10^4$, and the hysteresis windows are all oriented in the counterclockwise direction, demonstrating that the fabricated Pt-CN synaptic transistors possess high reproducibility. Under single-pulse excitation, the device generates pronounced EPSC/IPSC responses (Figs. 5(b) and 5(c) and Figs. S16(c) and S16(d) in the ESM), followed by exponential paired-pulse depression (PPD) (Fig. 5(c), characteristic of STP driven by rapid carrier trapping/detrapping at positively polarized Pt centers.

PPD is a representative form of short-term synaptic plasticity and a key mechanism of transient memory. It describes the reduced postsynaptic response to the second of two closely spaced stimuli. As shown in Fig. 5(d), when two pulses with 30 ms width and a 30 ms interval are applied, the IPSC triggered by the second pulse ($A_2$) is evidently smaller than that of the first ($A_1$), demonstrating clear PPD behavior.

This phenomenon occurs because holes trapped in the floating-

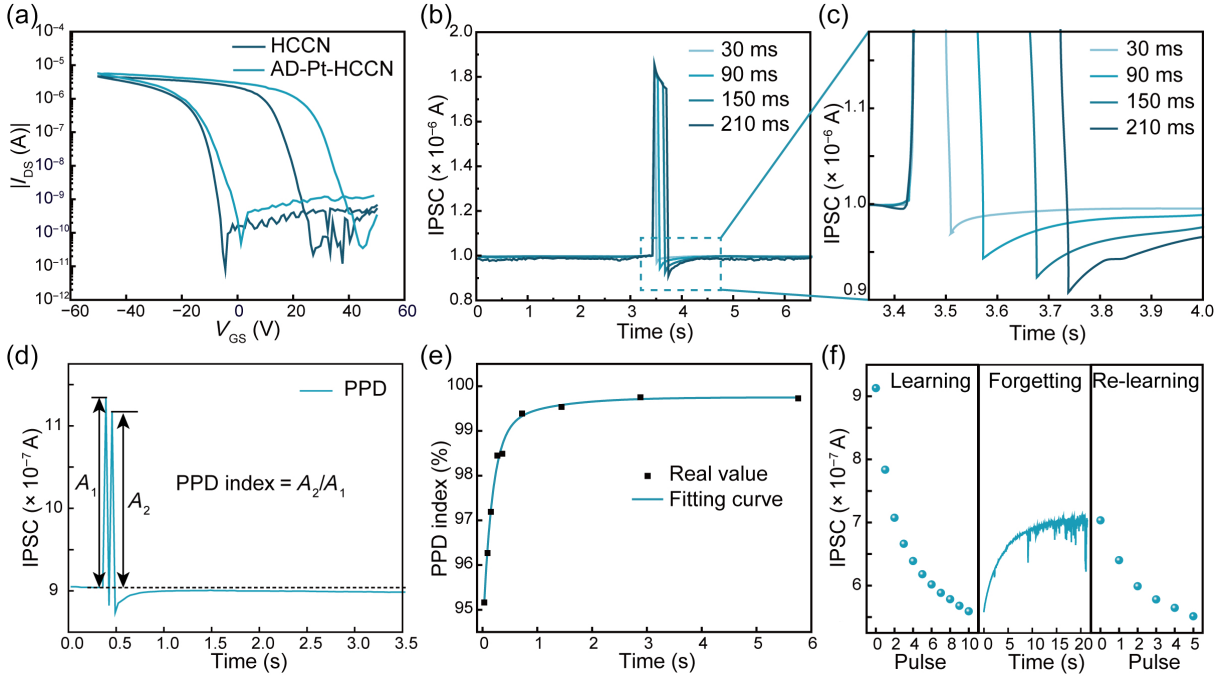



**Figure 5** Synaptic plasticity enabled by AD-Pt-HCCN. (a) Double-sweep transfer curves of the synaptic transistor device based on pristine HCCN and AD-Pt-HCCN measured at a $V_{DS}$ ($V_{DS}$ is the drain-to-source voltage applied between the drain and source electrodes of the transistor) of −10 V. (b) IPSC traces recorded at $V_{GS}$ = −5 V ($V_{GS}$ is the gate-to-source voltage applied between the gate and source electrodes of the transistor) under electrical pulses with different pulse widths. (c) Magnified view of the dashed box region in (b). (d) IPSC stimulated by two successive electric pulses (−5 V) with $\Delta t$ = 30 ms. (e) PPD index vs. pulse interval. (f) Learning–forgetting–relearning cycles.

gate layer after the first pulse do not fully recombine before the second arrives. The subsequent pulse thus induces additional electron trapping and alters channel charge accumulation, leading to a diminished response amplitude.

The PPD index is defined as

$$\text{PPD index} = \frac{A_2}{A_1} \times 100\% \quad (1)$$

As shown in Fig. 5(e), the PPD index approaches 100% as the inter-pulse interval increases, resembling the relaxation dynamics of biological synapses. Its dependence on $\Delta t$ (where $\Delta t$ is the time interval between two consecutive electrical pulses) follows a bi-exponential decay

$$\text{PPD index} = C_0 + C_1 e^{-\frac{\Delta t}{\tau_1}} + C_2 e^{-\frac{\Delta t}{\tau_2}} \quad (2)$$

where $C_0$ is the asymptotic baseline of the normalized PPD index and is fixed at 1 (i.e., 100%), while $C_1$ and $C_2$ represent the amplitudes of the fast and slow decay components, respectively. The relaxation constants ($\tau_1$ = 0.17 and $\tau_2$ = 0.98) indicate that the slow component is over an order of magnitude longer than the fast one.

With increasing pulse number or pulse width, the device exhibits a monotonic accumulation of IPSC (Figs. S16(e) and S16(f) in the ESM), enabling a smooth transition from short- to long-term modulation. The resulting LTD characteristics show excellent linearity and low cycle-to-cycle variation (Fig. 5(e)), while the learning–forgetting–relearning cycles (Fig. 5(f)) highlight the high reversibility and memory consolidation enabled by the Pt-engineered trapping network. In addition to electrical stimuli, robust optoelectronic plasticity is observed: IPSC increases systematically with optical power density and illumination duration (Figs. S16(g) and S16(h) in the ESM), demonstrating multimodal electro-optical synaptic tunability. Collectively, these results establish atomically dispersed Pt as a powerful modulation center that simultaneously optimizes synaptic gain, temporal dynamics, and multimodal responsiveness—providing a unified materials platform for high-performance neuromorphic computing.

Mechanistically, the energy-band alignment of the Si/$SiO_2$/AD-Pt-HCCN/PVP/PDVT-10 stack shown in Fig. 6(a) defines the bias-dependent operating states illustrated in Figs. 6(b) and 6(c). The asymmetric interfacial barrier landscape and the Pt-engineered trap states in AD-Pt-HCCN jointly govern charge storage and release under opposite gate polarities. Under positive gate bias (Fig. 6(b)), carriers are driven toward the PVP/PDVT-10 interface and become stabilized in Pt-associated trap states, resulting in efficient charge accumulation and long-lived potentiation. Under negative gate bias (Fig. 6(c)), the band profile favors detrapping and carrier extraction, thereby accelerating conductance decay and enabling efficient depression. In this way, the operational schematics in Figs. 6(b) and 6(c) directly reflect the band configuration introduced in Fig. 6(a) and provide a physically consistent picture for the observed polarity-dependent synaptic behavior. This polarity-responsive charge trapping/detrapping mechanism is further reflected in the hybrid electro-optical plasticity of the device: Optical pulses induce gradual conductance enhancement while electrical pulses trigger robust depression (Fig. 6(e)). The seamless integration of light-driven potentiation and voltage-driven depression establishes AD-Pt-HCCN as a dual-mode synaptic element uniquely suited for energy-efficient neuromorphic learning.

Leveraging these experimentally measured conductance states, a hybrid optoelectronic ANN was constructed to evaluate the device's computational performance (Fig. 6(d)). The ANN with multi-layer architecture achieves high digit recognition accuracy, as evidenced by a clear diagonal tendency in the confusion matrix (Fig. 6(f)), demonstrating reliable digit classification with minimal cross-category interference. The recognition accuracy rapidly converges to 98.6% (Fig. 6(g)), underscoring the device's suitability for hardware-implemented learning with excellent stability and weight reproducibility. Collectively, Fig. 6 highlights that the AD-Pt-HCCN synapse not only supports multimodal plasticity but also translates these physical weight states into high-fidelity ANN performance, marking a critical step toward practical neuromorphic hardware based on dry-processed atomically dispersed Pt systems.

## 4 Conclusions

In this work, we establish a scalable dry-state photoreduction strategy that enables the formation of stable, uniformly dispersed Pt single atoms on highly crystalline carbon nitride. By eliminating solvent- and ligand-derived interferences and suppressing nanoparticle nucleation, this method achieves a markedly enhanced Pt precursor conversion efficiency (70.5%) and constructs a unique quasi-fivefold Pt configuration environment. Combined XAFS, TA, XPS, TEM, and DFT analyses reveal that this coordination motif modulates the local electronic structure, removes Schottky-type interfacial barriers, and creates dense electron-transport pathways that substantially enhance charge separation and extraction. Importantly, the superior carrier-separation capability arises from the synergy between the increased density of accessible Pt active centers and the enhanced interfacial charge-transfer kinetics enabled by atomic Pt dispersion. These atomic-level advantages translate into significantly improved photocatalytic hydrogen evolution activity and long-term reaction stability. Beyond catalysis, the same Pt sites act as dynamic charge-trapping centers that endow the AD-Pt-HCCN synaptic transistor with strong excitatory responses, short- and long-term plasticity, and programmable analog weight updates suitable for hardware-level neural network inference.

More broadly, this dry-state single-atom engineering method provides a universal, ligand-free route for constructing high-density atomic active sites with precisely tailored electronic structures. Owing to its solvent-free and precursor-confined nature, the approach is readily extendable to other transition metals (e.g., Au, Ag, Ni, Co, Ru, and Ir), offering a powerful materials platform for diverse catalytic and electronic applications. The intrinsic photo- and electro-responsive characteristics of these single-atom architectures also make them promising candidates for optoelectronic synapses, memristive devices, and multimodal artificial-vision systems. Furthermore, the dry anchoring strategy is fully compatible with flexible and transparent substrates, opening an avenue toward next-generation deformable or wearable neuromorphic and catalytic devices. By demonstrating that atomically dispersed catalytic centers can simultaneously function as neuromorphic modulation elements, this study establishes a new paradigm for energy-intelligence integrated materials. The findings lay a conceptual and technological foundation for intelligent catalytic platforms, adaptive optoelectronic systems, and hybrid artificial-synapse architectures that bridge sustainable energy conversion with brain-inspired computation. At the scientific level,

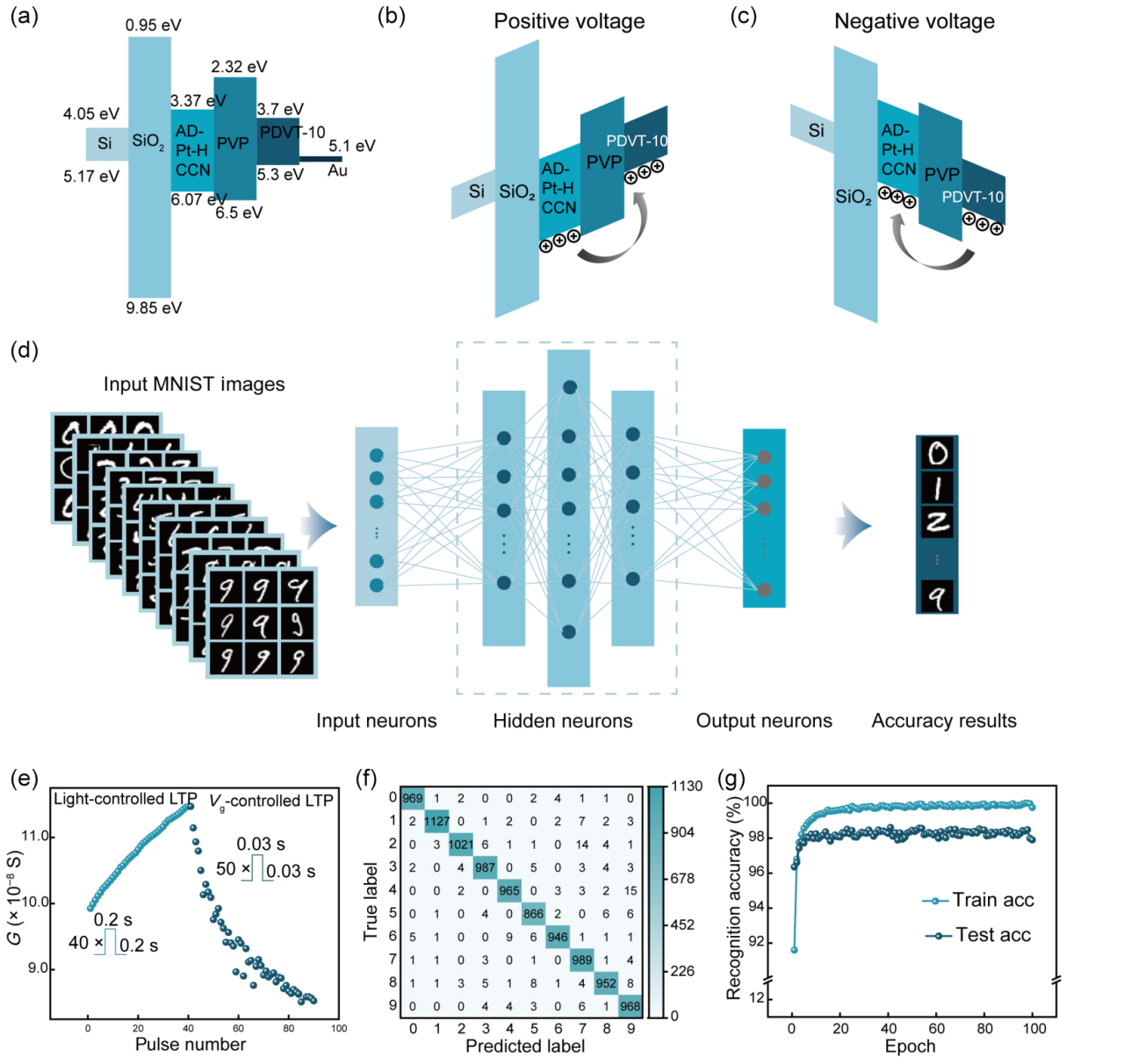



**Figure 6** Optoelectronic synaptic operation and ANN recognition performance of the AD-Pt-HCCN hybrid neuromorphic device. (a) Energy-band structure of the as-fabricated Si/$SiO_2$/AD-Pt-HCCN/PVP/PDVT-10 stack. ((b) and (c)) Bias-dependent operating schematics derived from the band alignment in (a), illustrating charge accumulation/trapping under positive gate bias and charge detrapping/extraction under negative gate bias. (d) Diagram of ANN neural networks. (e) The optical potentiation (40 light pulses, 0.2 s, 0.6 mW·cm$^{-2}$) and electrical depression (50 voltage pulses, 30 ms, $V_{GS}$ = −10 V) characteristics of device. (f) Test set confusion matrix of optoelectronic hybrid ANN. Each row of the matrix represents the desired output digit, and each column represents the predicted output number. (g) Recognition rate as a function of training epochs.

this work addresses a shared interfacial charge-regulation problem in polymeric semiconductors, rather than merely combining two application scenarios in a single study.

**Electronic Supplementary Material**: Supplementary material (further details of material fabrication; HAADF-STEM, TEM, EDS, XRD, XPS, EXAFS, FTIR, UV–Vis, and femtosecond transient absorption measurements; DFT structural calculations; ICP-AES determination of Pt loading; photocatalytic hydrogen evolution and stability tests; and synaptic transistor characterization) is available in the online version of this article at https://doi.org/10.26599/NR.2026.94908796.

## Data availability

All data needed to support the conclusions in the paper are presented in the manuscript and the Electronic Supplementary Material. Additional data related to this paper may be requested from the corresponding author upon request.

## Acknowledgements

We thank the Recruitment Program of Global Experts; the National Natural Science Foundation of China (No. 62175033); China Scholarship Council (No. 202106650017); the Olle Engkvist foundation (No. SOEB-2015/167); the Swedish Energy Agency (No. 46641-1), and the Key Laboratory for Ultrafine Materials of the

Ministry of Education at East China University of Science and Technology for their financial support. Part of the work was performed at the Ångström Microstructure Laboratory (myfab), Uppsala University. Z. H. Z. and W. L. thank for the financially supported by the Swedish Research Council (Nos. VR-2016-06014 and VR-2020-04410) and J. Gust. Richert stiftelse, Sweden (No. 2021-00665). M. G. thanks the Åforsk foundation (No. 21-384) for financial support and the strategic research initiative STandUP for Energy. We also thank Michael Haumann, Holger Dau, Ivo Zizak, and Götz Schuck for assistance with XAS measurements at BESSY II, HZB. The computational resources are provided by the Swedish National Infrastructure for Computing (SNIC) at the National Supercomputer Centre (NSC) in Linköping, Sweden. We would like to express our special thanks to Shengming Wu (Chaos Shield Technology Co., Ltd., Fuzhou High-Tech Zone, 350100, China) for his support in ANN.

## Declaration of competing interest

All the contributing authors report no conflict of interests in this work.

## Author contribution statement

Y. F. L.: Conceptualization, methodology, investigation, data curation, validation, formal analysis, writing – original draft. X. X. Z.: Conceptualization, methodology, investigation, data curation, validation, formal analysis, writing – original draft. W. H. S.: Conceptualization, methodology, investigation, data curation, validation, formal analysis, writing – original draft. C. Y. Y.: Investigation, validation. J. W. P.: Investigation, validation. M. G.: Investigation, validation. A. H.: Investigation, validation. E. G. W.: Investigation, resources. X. F.: Investigation, validation. Z. H. Z.: Investigation, formal analysis. R. A.: Formal analysis, validation. W. L.: Formal analysis, validation. H. P. C.: Supervision, project administration, funding acquisition, writing – review & editing. J. F. Z.: Supervision, project administration, funding acquisition, writing – review & editing. Y. H. Z.: Conceptualization, supervision, project administration, funding acquisition, writing – review & editing. All authors have read and approved the final manuscript.

## Use of AI statement

None.

## References

[1] Ren, W.; Cheng, J. J.; Ou, H. H.; Huang, C. J.; Titirici, M. M.; Wang, X. C. Enhancing visible-light hydrogen evolution performance of crystalline carbon nitride by defect engineering. *ChemSusChem* **2019**, *12*, 3257–3262.

[2] Zhang, X. H.; Liu, D.; Liu, S.; Cai, Y. J.; Shan, L. T.; Chen, C.; Chen, H. M.; Liu, Y. Q.; Guo, T. L.; Chen, H. P. Toward intelligent display with neuromorphic technology. *Adv. Mater.* **2024**, *36*, 2401821.

[3] Chaurasiya, R.; Shih, L. C.; Chen, K. T.; Chen, J. S. Emerging higher-order memristors for bio-realistic neuromorphic computing: A review. *Mater. Today* **2023**, *68*, 356–376.

[4] Zhang, Q.; Jin, T. Y.; Ye, X.; Geng, D. C.; Chen, W.; Hu, W. P. Organic field effect transistor-based photonic synapses: Materials, devices, and applications. *Adv. Funct. Mater.* **2021**, *31*, 2106151.

[5] Gou, K. Y.; Li, Y. R.; Song, H. L.; Lu, R.; Jiang, J. Optimization strategy of the emerging memristors: From material preparation to device applications. *iScience* **2024**, *27*, 111327.

[6] He, Y. L.; Zhu, L.; Zhu, Y.; Chen, C. S.; Jiang, S. S.; Liu, R.; Shi, Y.; Wan, Q. Recent progress on emerging transistor-based neuromorphic devices. *Adv. Intell. Syst.* **2021**, *3*, 2000210.

[7] Xu, N.; Wang, Y. F.; Huo, Z. W.; Yu, J. R.; Yang, J. H.; Wang, Z. L.; Sun, Q. J. Flexible and self-powered paper-based artificial synapse for neuromorphic computing and 3d information transmission. *Nano Res. Energy* **2025**, *4*, e9120187.

[8] Jana, R.; Bhunia, R.; Paramanik, S.; Giri, K.; Chowdhury, A. Conductive islands assisted resistive switching in biomimetic artificial synapse for associative learning and image recognition. *Adv. Funct. Mater.* **2025**, *35*, 2412804.

[9] Li, J.; Yang, Y. H.; Chen, Q.; Zhu, W. Q.; Zhang, J. H. Aqueous-solution-processed proton-conducting carbon nitride/polyvinylpyrrolidone composite electrolytes for low-power synaptic transistors with learning and memory functions. *J. Mater. Chem. C* **2020**, *8*, 4065–4072.

[10] Qiao, F. Photoelectrocatalytic hydrogen production: Hydrogen production principle, performance optimization strategy, application and prospect. *Nano Res. Energy* **2025**, *4*, e9120132.

[11] Yap, F. M.; Sheng Ling, G. Z.; Su, B. J.; Loh, J. Y.; Ong, W.-J. Recent advances in structural modification on graphitic carbon nitride (g-$C_3N_4$)-based photocatalysts for high-efficiency photocatalytic $H_2O_2$ production. *Nano Res. Energy* **2024**, *3*, e9120091.

[12] Liu, M. H.; Zhang, G. G.; Liang, X. C.; Pan, Z. M.; Zheng, D. D.; Wang, S. B.; Yu, Z. Y.; Hou, Y. D.; Wang, X. C. Rh/$Cr_2O_3$ and $CoO_x$ cocatalysts for efficient photocatalytic water splitting by poly (triazine imide) crystals. *Angew. Chem., Int. Ed.* **2023**, *62*, e202304694.

[13] Chen, J. Z.; Wu, X. J.; Yin, L. S.; Li, B.; Hong, X.; Fan, Z. X.; Chen, B.; Xue, C.; Zhang, H. One-pot synthesis of CdS nanocrystals hybridized with single-layer transition-metal dichalcogenide nanosheets for efficient photocatalytic hydrogen evolution. *Angew. Chem., Int. Ed.* **2015**, *54*, 1210–1214.

[14] Zong, X.; Yan, H. J.; Wu, G. P.; Ma, G. J.; Wen, F. Y.; Wang, L.; Li, C. Enhancement of photocatalytic $H_2$ evolution on CdS by loading $MoS_2$ as cocatalyst under visible light irradiation. *J. Am. Chem. Soc.* **2008**, *130*, 7176–7177.

[15] Sun, W. H.; Ahmed, T.; Elbouazzaoui, K.; Edvinsson, T.; Zheng, Y. H.; Zhu, J. F. Facile fabrication of AgBr/HCCN hybrids with Z-scheme heterojunction for efficient photocatalytic hydrogen evolution. *Appl. Surf. Sci.* **2024**, *651*, 159292.

[16] Wang, X. C.; Maeda, K.; Thomas, A.; Takanabe, K.; Xin, G.; Carlsson, J. M.; Domen, K.; Antonietti, M. A metal-free polymeric photocatalyst for hydrogen production from water under visible light. *Nat. Mater.* **2009**, *8*, 76–80.

[17] Cao, Y. J.; Chen, S.; Luo, Q. Q.; Yan, H.; Lin, Y.; Liu, W.; Cao, L. L.; Lu, J. L.; Yang, J. L.; Yao, T. et al. Atomic-level insight into optimizing the hydrogen evolution pathway over a $Co_1$–$N_4$ single-site photocatalyst. *Angew. Chem., Int. Ed.* **2017**, *56*, 12191–12196.

[18] Lu, Y. F.; Wang, W. S.; Cheng, H. R.; Qiu, H. J.; Sun, W. H.; Fang, X.; Zhu, J. F.; Zheng, Y. H. Bamboo-charcoal-loaded graphitic carbon nitride for photocatalytic hydrogen evolution. *Int. J. Hydrogen Energy* **2022**, *47*, 3733–3740.

[19] Cheng, H. R.; Sun, W. H.; Lu, Y. F.; Li, H. H.; Su, W. Y.; Zhang, J.; Guo, T. L.; Li, F. S.; Francis, P. S.; Zheng, Y. H. Hot electrons in carbon nitride with ultralong lifetime and their application in reversible dynamic color displays. *Cell Rep. Phys. Sci.* **2021**, *2*, 100516.

[20] Chen, P. Y.; Peng, X. C.; Yu, S. M. NeuroSim: A circuit-level macro model for benchmarking neuro-inspired architectures in online learning. *IEEE Trans. Comput. Aided Des. Integr. Circuits Syst.* **2018**, *37*, 3067–3080.

[21] Duan, Q. X.; Jing, Z. K.; Zou, X. L.; Wang, Y. H.; Yang, K.; Zhang, T.; Wu, S.; Huang, R.; Yang, Y. C. Spiking neurons with spatiotemporal dynamics and gain modulation for monolithically integrated memristive neural networks. *Nat. Commun.* **2020**, *11*, 3399.

[22] Han, J. L.; Ma, D.; Jiang, L. X.; Zhang, Y.; Dong, M. Q.; Deng, Y. F.;

Geng, Y. H.; Huang, R.; Xu, C.; Zheng, X. et al. Ultra-sensitive negative photoconductivity transistors via long-afterglow doping for all-optical encryption. *Adv. Mater.* **2026**, *38*, e14723.

[23] Huang, Y. X.; Yang, W. X.; Zhou, P. K.; Liu, N. Y.; Xu, S. M.; Qiu, J. W.; Zeng, T.; Wu, C. X.; Huang, W. G.; Lin, W. et al. Intermolecular hydrogen-bond stabilized 1D pyrene-based covalent organic framework for advanced memory devices and neuromorphic computing. *Adv. Funct. Mater.* **2025**, *35*, 2505890.

[24] Lan, S. Q.; Zhong, J. F.; Chen, J. W.; He, W. X.; He, L. H.; Yu, R. J.; Chen, G. X.; Chen, H. P. An optoelectronic synaptic transistor with efficient dual modulation by light illumination. *J. Mater. Chem. C* **2021**, *9*, 3412–3420.

[25] Lee, H.; Cho, J.; Jin, M.; Lee, J. H.; Lee, C.; Kim, J.; Lee, J.; Shin, J. C.; Yoo, J.; Lee, E. et al. Electrochemical analysis of ion effects on electrolyte-gated synaptic transistor characteristics. *ACS Nano* **2024**, *18*, 5383–5395.

[26] Zhao, W. X.; Lin, Z. X.; Chen, H.; Xu, S.; Chen, E. G.; Guo, T. L.; Ye, Y.; Chen, H. P. Perovskite-doped modulated color-selective photosynaptic transistors for target object recognition. *Nano Lett.* **2024**, *24*, 9937–9945.

[27] Deng, X.; Wang, S. Q.; Liu, Y. X.; Zhong, N.; He, Y. H.; Peng, H.; Xiang, P. H.; Duan, C. G. A flexible Mott synaptic transistor for nociceptor simulation and neuromorphic computing. *Adv. Funct. Mater.* **2021**, *31*, 2101099.

[28] Ou, H. H.; Lin, L. H.; Zheng, Y.; Yang, P. J.; Fang, Y. X.; Wang, X. C. Tri-s-triazine-based crystalline carbon nitride nanosheets for an improved hydrogen evolution. *Adv. Mater.* **2017**, *29*, 1700008.

[29] Li, X. G.; Bi, W. T.; Zhang, L.; Tao, S.; Chu, W. S.; Zhang, Q.; Luo, Y.; Wu, C. Z.; Xie, Y. Single-atom Pt as Co-catalyst for enhanced photocatalytic $H_2$ evolution. *Adv. Mater.* **2016**, *28*, 2427–2431.

[30] Risch, M.; Klingan, K.; Heidkamp, J.; Ehrenberg, D.; Chernev, P.; Zaharieva, I.; Dau, H. Nickel-oxido structure of a water-oxidizing catalyst film. *Chem. Commun.* **2011**, *47*, 11912–11914.

[31] Sun, W. H.; Cheng, H. R.; Zhang, J.; Fang, X.; Chen, W. K.; Zhu, J. F.; Zheng, Y. H. Allochroic platinum/carbon nitride with photoactivated Ohmic contact for efficient visible-light photocatalytic hydrogen evolution. *Chem. Eng. J.* **2023**, *462*, 142337.

[32] Zhou, P.; Lv, F.; Li, N.; Zhang, Y. L.; Mu, Z. J.; Tang, Y. H.; Lai, J. P.; Chao, Y. G.; Luo, M. C.; Lin, F. et al. Strengthening reactive metal–support interaction to stabilize high-density Pt single atoms on electron-deficient g-$C_3N_4$ for boosting photocatalytic $H_2$ production. *Nano Energy* **2019**, *56*, 127–137.

[33] Lazaar, N.; Qin, S. S.; Hamrouni, A.; Lachheb, H.; Kolařík, J.; Zhou, X. M.; Schmuki, P. Reactive deposition of Pt single atoms on g-$C_3N_4$: Effect of Pt-precursors. *Nanoscale* **2025**, *17*, 23940–23947.

[34] Zhao, Y. J.; Min, X.; Ding, Z. P.; Chen, S.; Ai, C. Z.; Liu, Z. L.; Yang, T. Z.; Wu, X. W.; Liu, Y. G.; Lin, S. W. et al. Metal-based nanocatalysts via a universal design on cellular structure. *Adv. Sci.* **2020**, *7*, 1902051.

[35] Lin, L. H.; Ou, H. H.; Zhang, Y. F.; Wang, X. C. Tri-s-triazine-based crystalline graphitic carbon nitrides for highly efficient hydrogen evolution photocatalysis. *ACS Catal.* **2016**, *6*, 3921–3931.

[36] Yang, L. P.; Dong, G. H.; Jacobs, D. L.; Wang, Y. H.; Zang, L.; Wang, C. Y. Two-channel photocatalytic production of $H_2O_2$ over g-$C_3N_4$ nanosheets modified with perylene imides. *J. Catal.* **2017**, *352*, 274–281.

[37] Yu, F. Y.; Lang, Z. L.; Yin, L. Y.; Feng, K.; Xia, Y. J.; Tan, H. Q.; Zhu, H. T.; Zhong, J.; Kang, Z. H.; Li, Y. G. Pt–O bond as an active site superior to $Pt^0$ in hydrogen evolution reaction. *Nat. Commun.* **2020**, *11*, 490.

[38] Luo, B.; Song, R.; Jing, D. W. Significantly enhanced photocatalytic hydrogen generation over graphitic carbon nitride with carefully modified intralayer structures. *Chem. Eng. J.* **2018**, *332*, 499–507.

[39] Yu, H. J.; Shi, R.; Zhao, Y. X.; Bian, T.; Zhao, Y. F.; Zhou, C.; Waterhouse, G. I. N.; Wu, L. Z.; Tung, C. H.; Zhang, T. R. Alkali-assisted synthesis of nitrogen deficient graphitic carbon nitride with tunable band structures for efficient visible-light-driven hydrogen evolution. *Adv. Mater.* **2017**, *29*, 1605148.

[40] Ou, M.; Tu, W. G.; Yin, S. M.; Xing, W. N.; Wu, S. Y.; Wang, H. J.; Wan, S. P.; Zhong, Q.; Xu, R. Amino-assisted anchoring of $cspbbr_3$ perovskite quantum dots on porous g-$C_3N_4$ for enhanced photocatalytic $CO_2$ reduction. *Angew Chem., Int. Ed.* **2018**, *57*, 13570–13574.

[41] Ding, J.; Xu, W.; Wan, H.; Yuan, D. S.; Chen, C.; Wang, L.; Guan, G. F.; Dai, W. L. Nitrogen vacancy engineered graphitic $C_3N_4$-based polymers for photocatalytic oxidation of aromatic alcohols to aldehydes. *Appl. Catal. B: Environ.* **2018**, *221*, 626–634.

[42] Liu, D.; Shen, J. N.; Xie, Y. Y.; Qiu, C. W.; Zhang, Z. Z.; Long, J. L.; Lin, H. X.; Wang, X. X. Metallic Pt and $PtO_2$ dual-cocatalyst-loaded binary composite RGO–$CN_x$ for the photocatalytic production of hydrogen and hydrogen peroxide. *ACS Sustainable Chem. Eng.* **2021**, *9*, 6380–6389.

[43] Wei, H. H.; Huang, K.; Zhang, L.; Ge, B. H.; Wang, D.; Lang, J. L.; Ma, J. Y.; Wang, D.; Zhang, S.; Li, Q. Y. et al. Ice melting to release reactants in solution syntheses. *Angew. Chem., Int. Ed.* **2018**, *57*, 3354–3359.

[44] Gao, G. P.; Jiao, Y.; Waclawik, E. R.; Du, A. J. Single atom (Pd/Pt) supported on graphitic carbon nitride as an efficient photocatalyst for visible-light reduction of carbon dioxide. *J. Am. Chem. Soc.* **2016**, *138*, 6292–6297.

[45] Li, Y.; Li, B. H.; Zhang, D. N.; Cheng, L.; Xiang, Q. J. Crystalline carbon nitride supported copper single atoms for photocatalytic $CO_2$ reduction with nearly 100% CO selectivity. *ACS Nano* **2020**, *14*, 10552–10561.

[46] Lazaar, N.; Wu, S. M.; Qin, S. S.; Hamrouni, A.; Bikash Sarma, B.; Doronkin, D. E.; Denisov, N.; Lachheb, H.; Schmuki, P. Single-atom catalysts on $C_3N_4$: Minimizing single atom Pt loading for maximized photocatalytic hydrogen production efficiency. *Angew. Chem., Int. Ed.* **2025**, *64*, e202416453.

[47] Yadav, D. K.; Latiyan, S.; Devan, R. S.; Urkude, R. R.; Rajput, P.; Singh, A.; Deka, S. Breaking barriers: Synergistic interactions between Pt single atoms and nitrogen-rich g-$C_3N_4$ for maximized photocatalytic hydrogen production. *Small* **2025**, *21*, 2503843.

[48] Liu, D. J.; Zhang, C. Y.; Shi, J. W.; Jin, X. D.; Liu, W.; Liu, M. C.; Chen, Y. B.; Guo, L. J. Modulating local coordination structure over single Pt atom to optimize adsorption behavior for high-efficiency photocatalytic $H_2$ production. *Appl. Catal. B: Environ. Energy* **2025**, *361*, 124655.

[49] Zhang, D. L.; Zhang, C.; Zhao, G. F.; Gao, Y. S.; Zhuang, T.; Lv, Z. G. Single-atom Pt supported on defective graphitic carbon nitride for efficient photocatalytic hydrogen production. *Chem. Eng. J.* **2025**, *505*, 159567.

[50] Zeng, Z. X.; Quan, X.; Yu, H. T.; Chen, S.; Zhang, Y. B.; Zhao, H. M.; Zhang, S. S. Carbon nitride with electron storage property: Enhanced exciton dissociation for high-efficient photocatalysis. *Appl. Catal. B: Environ.* **2018**, *236*, 99–106.

[51] Kasap, H.; Caputo, C. A.; Martindale, B. C. M.; Godin, R.; Lau, V. W. H.; Lotsch, B. V.; Durrant, J. R.; Reisner, E. Solar-driven reduction of aqueous protons coupled to selective alcohol oxidation with a carbon nitride-molecular Ni catalyst system. *J. Am. Chem. Soc.* **2016**, *138*, 9183–9192.

[52] Tan, H.; Gu, X. M.; Kong, P.; Lian, Z.; Li, B.; Zheng, Z. F. Cyano group modified carbon nitride with enhanced photoactivity for selective oxidation of benzylamine. *Appl. Catal. B: Environ.* **2019**, *242*, 67–75.

[53] Xiang, X. L.; Zhang, L. Y.; Luo, C.; Zhang, J. J.; Cheng, B.; Liang, G. J.; Zhang, Z. Y.; Yu, J. G. Ultrafast electron transfer from CdS quantum dots to atomically-dispersed Pt for enhanced $H_2$ evolution and value-added chemical synthesis. *Appl. Catal. B: Environ.* **2024**, *340*, 123196.

[54] Gao, R. T.; Zhang, J. W.; Nakajima, T.; He, J. L.; Liu, X. H.; Zhang, X. Y.; Wang, L.; Wu, L. M. Single-atomic-site platinum steers

photogenerated charge carrier lifetime of hematite nanoflakes for photoelectrochemical water splitting. *Nat. Commun.* **2023**, *14*, 2640.

[55] Sun, W. H.; Zhu, J. F.; Zheng, Y. H. Graphitic carbon nitride heterojunction photocatalysts for solar hydrogen production. *Int. J. Hydrogen Energy* **2021**, *46*, 37242–37267.

[56] Huang, K. L.; Li, C. H.; Yang, J.; Zheng, R.; Wang, W. T.; Wang, L. Platinum nanodots modified Nitrogen-vacancies g-$C_3N_4$ Schottky junction for enhancing photocatalytic hydrogen evolution. *Appl. Surf. Sci.* **2022**, *581*, 152298.

[57] Zeng, D. D.; Li, Y. X. Precisely loading Pt on Tb4O7/CN heterojunction for efficient photocatalytic overall water splitting: Design and mechanism. *Appl. Catal. B: Environ.* **2024**, *342*, 123393.

[58] Yang, L.; Grzeschik, R.; Jiang, P.; Yu, L. F.; Hu, C. J.; Du, A. X.; Schlücker, S.; Xie, W. Tuning the electronic properties of platinum in hybrid-nanoparticle assemblies for use in hydrogen evolution reaction. *Angew. Chem., Int. Ed.* **2023**, *62*, e202301065.

[59] Li, S. Z.; Miyazaki, T.; Nakata, A. Theoretical search for characteristic atoms in supported gold nanoparticles: A large-scale DFT study. *Phys. Chem. Chem. Phys.* **2024**, *26*, 20251–20260.

[60] Li, Y. H.; Xing, J.; Chen, Z. J.; Li, Z.; Tian, F.; Zheng, L. R.; Wang, H. F.; Hu, P.; Zhao, H. J.; Yang, H. G. Unidirectional suppression of hydrogen oxidation on oxidized platinum clusters. *Nat. Commun.* **2013**, *4*, 2500.

This is an open access article under the terms of the Creative Commons Attribution 4.0 International License (CC BY 4.0, https://creativecommons.org/licenses/by/4.0/).

© The Author(s) 2026. Published by Tsinghua University Press.